High Spatial Resolution Analysis of Electric Currents Induced in Man by ELF Magnetic Fields

Weiguo Xi and Maria A. Stuchly
Department of Electrical and Computer Engineering
University of Victoria, Victoria, BC, Canada
V8W 3P6

Abstract This paper presents the formulation of the impedance network method that allows computation of the arbitrary injection currents on the boundary of a selected sub-region for an analysis of induced electric current distributions inside the human body exposed to extremely low frequency magnetic fields. The obtained formulation provides a high resolution modeling of a local region of interest without using an excessively large number of computational cells. The iterative equations for outer and inner nodes are derived in detail. Solutions for a double-layered sphere are then calculated to verify the derived equations. The errors involved in the calculation are also examined. To illustrate the method, its application to computations of the induced currents in the human head is described.

Introduction

Knowledge of the spatial distribution of the electric currents and fields induced in the human body by extremely low frequency (ELF) magnetic fields is important in the assessment of potential health hazards to people [1,2]. A high spatial resolution of these fields is also very useful in some medical applications, e.g., neural stimulation [3]. Although this problem for homogeneous biological bodies is well understood, considerable work remains to be done in the development of numerical methods and algorithms for heterogeneous systems. Among the methods developed for electromagnetic (EM) problems, two differential equation-based methods: the time-domain finite difference method (FDTD) and the impedance or admittance network method, have been found effective for modeling of heterogeneous and complicated 3D bodies representing biological subjects [4]. At ELF, the problem is a quasi-static one as the displacement current is negligible compared to the conduction current. This, together with the fact that a biological system does not perturb an exposing magnetic field, makes the impedance network method especially attractive for the ELF calculation.

As in any other numerical method for EM problems, the impedance method starts with discretizing the space analyzed into computational cells. With large memories (16-64 Mbytes) increasingly available on computers today up to 1 million cells can be routinely handled. A reasonable representation of the human anatomy and its surroundings can therefore be obtained. However, the computing time increases almost exponentially with the number of unknowns. As a result, an increase in the number of the computational cells leads to demands of a computing speed not available in most computers. To illustrate the problem, we evaluated the calculation of a double-layered sphere on an HP 9000/700 workstation. The computation using about 70,000 cubical cells takes about 5 minutes of CPU time and 800 iterations before it reaches convergence. When, to model the curved interfaces more accurately, the cell size is reduced by half in each dimension, resulting in 8 times more of computational cells, i.e., 560,000 cells, convergence is obtained after about 3,600 iterations and 160 minutes of CPU time. Moreover, to model the detailed anatomy and morphology of a whole human body, one needs much more than 1 million computational cells. This is a formidable task in terms of both the memory and the computing speed requirements.

There are many practical situations where high resolution modeling is of interest for only a certain part of the body. For example, such situations arise in case of the exposure evaluation of the head to the magnetic field produced by a hair-drier, or the arm from a hand-held drill. In these situations and others, a finer mesh can be chosen without leading to an excessively large number of cells in any single computation. In previous work, the sub-region was detached from the whole body and analyzed alone [5,6]. Dependent on the exposure situation, the results from such an analysis may be questionable due to the neglect of the injection currents on the boundary where the sub-region is detached.

In this paper, a new approach for the sub-region analysis with a high spatial resolution is presented. In this approach, the injection currents on the sub-region boundary are taken into account by using the previously

computed results for the whole-body as the sub-region boundary values. The formulation involved in the boundary condition is described and verified by modeling a double-layered sphere. Finally, this approach is applied to the calculation of the induced currents in the human head in uniform 60 Hz magnetic fields.

Formulation of Sub-Region Analysis

In the impedance method, at ELF a biological body is represented by a 3D resistance network in which each parallelepiped volume shown in Fig.1(a) is equivalent to three resistances $R_x^{i,j,k}$, $R_y^{i,j,k}$ and $R_z^{i,j,k}$ associated with the network node (i,j,k) as shown in Fig.1(b). The resistances are calculated as [7]:

$$R_m^{i,j,k} = \Delta_m/(S_m\sigma_m^{i,j,k}) \quad (m=x,y,z) \tag{1}$$

where Δ_m is the cell length in the m-th direction, S_m is the area of the cell surface perpendicular to the m-th axis, and $\sigma_m^{i,j,k}$ is the cell electrical conductivity in the m-th direction. For each node, three line currents: $\hat{i}_x$, $\hat{i}_y$ and $\hat{i}_z$, and three loop currents: I_x, I_y and I_z are defined in Fig.1(c). Once the loop currents are known, the line current through each resistance element can be obtained by summing up the four loop currents which are common to that resistance element. As illustrated in Fig.1(d),

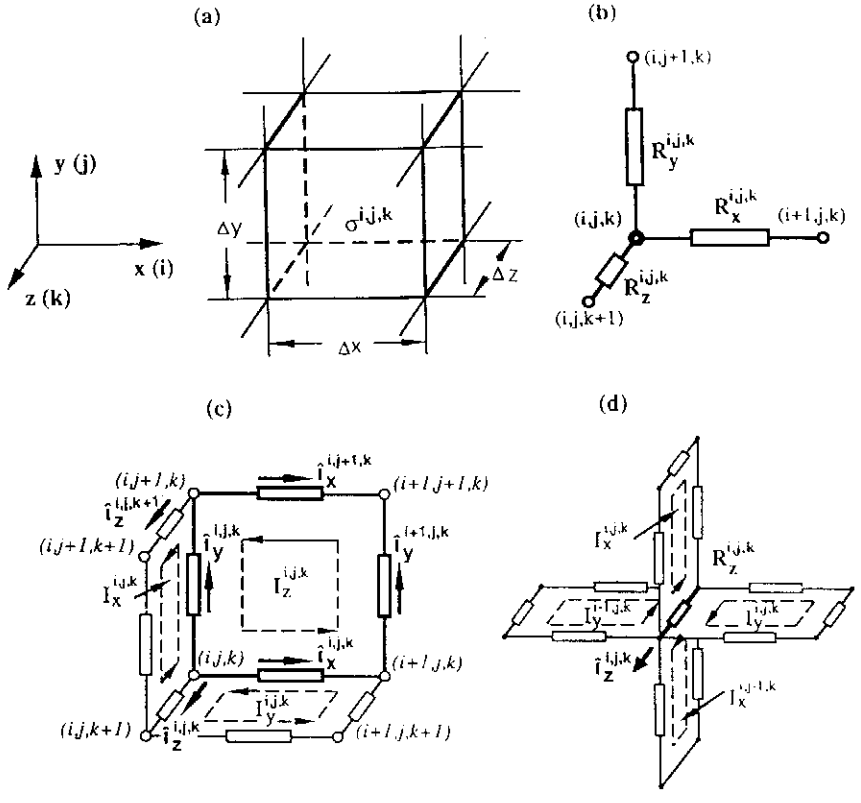

Figure 1. Cell impedance and current definition for the impedance network method.
(a) a parallelepiped tissue volume of the body forming a computation cell (i,j,k);
(b) the three directional impedances associated with node (i,j,k);
(c) the three line currents and loop currents, $\hat{i}_m$ and I_m (m=x,y,z), defined for node (i,j,k);
(d) the line current $\hat{i}_z^{i,j,k}$ composed of the superposition of four loop currents flowing through the resistance $R_z^{i,j,k}$.

the line current through $R_z^{i,j,k}$ can be expressed by the loop currents as

$$\hat{i}_z^{i,j,k} = -I_x^{i,j,k} + I_x^{i,j-1,k} + I_y^{i,j,k} - I_y^{i-1,j,k} \tag{2}$$

Similarly, $\hat{i}_x^{i,j,k}$ and $\hat{i}_y^{i,j,k}$ can be found to be

$$\hat{i}_x^{i,j,k} = -I_y^{i,j,k} + I_y^{i,j,k-1} + I_z^{i,j,k} - I_z^{i,j-1,k} \tag{3}$$

and

$$\hat{i}_y^{i,j,k} = -I_z^{i,j,k} + I_z^{i-1,j,k} + I_x^{i,j,k} - I_x^{i,j,k-1} \tag{4}$$

respectively. Applying Kirchhoff's voltage equation to each loop associated with node (i,j,k), say the z-loop in Fig.1(c), the following relationship is obtained

$$R_x^{i,j,k}\hat{i}_x^{i,j,k}+R_y^{i+1,j,k}\hat{i}_y^{i+1,j,k}-R_x^{i,j+1,k}\hat{i}_x^{i,j+1,k} -R_y^{i,j,k}\hat{i}_y^{i,j,k} = emf_z^{i,j,k} \quad (5)$$

where $emf_z^{i,j,k}$ is the electromotive force generated by a magnetic field perpendicular to the loop

$$emf_z^{i,j,k} = \omega B_z^{i,j,k} S_z \quad (6)$$

and $\omega = 2\pi f$, where f is the frequency and B is the magnetic flux density.
Substituting Eqs.(3) and (4) into Eq.(5), $I_z^{i,j,k}$ can be solved as

$$\begin{aligned} I_z^{i,j,k} = [&emf_z^{i,j,k} - R_x^{i,j,k}(I_y^{i,j,k-1}-I_y^{i,j,k}-I_z^{i,j-1,k}) \\ &-R_x^{i,j+1,k}(I_y^{i,j+1,k}-I_y^{i,j+1,k-1}-I_z^{i,j+1,k}) \\ &-R_y^{i,j,k}(I_x^{i,j,k-1}-I_x^{i,j,k}-I_z^{i-1,j,k}) - \\ &-R_y^{i+1,j,k}(I_x^{i+1,j,k}-I_x^{i+1,j,k-1}-I_z^{i+1,j,k})] \\ &/[R_x^{i,j,k}+R_x^{i,j+1,k}+R_y^{i,j,k}+R_y^{i+1,j,k}] \end{aligned} \quad (7)$$

Similar equations can be derived for $I_x^{i,j,k}$ and $I_y^{i,j,k}$. More details can be found elsewhere [7]. It should be pointed out that the (i,j,k) referred to so far is an inner node, that is, a node surrounded by non-boundary nodes. For outer nodes, some of the line currents in Eq.(5) are the boundary values and should not be converted into the loop currents. Eq.(5) is still valid for outer nodes, however, their final loop current equations differ from those for inner nodes.

Let's consider the generic parallelepiped region shown in Fig.2a. This region can representi either a biological body and its surrounding space or a sub-region identified from the whole body for the purpose of a high spatial resolution analysis. On its six surfaces: left (i=1), right (i=n_x), bottom (j=1), top (j=n_y), rear (k=1) and front (k=n_z), line currents are assumed to be known. In the sub-region analysis, the line current density on the boundary can be obtained by interpolating the results from the whole region analysis. The line currents on the boundary are sometimes called injection currents, however, they may also flow outward or parallel to the boundary as shown in Fig.2(a).

All the outer nodes at which the loop equations are formulated differently from those for inner nodes are classified in Table 1. They do not cover all the outer nodes because the loop currents at some outer nodes are not needed for inner node calculations, such as those loop currents parallel to the boundary surface. According to the number of the boundary line currents employed, the outer nodes in Table 1 fall into three categories: those on the upper surfaces, those along the edges and those on the lower surfaces. The corner node (n_x-1,n_y-1,n_z-1) is included in the case of the edge nodes.

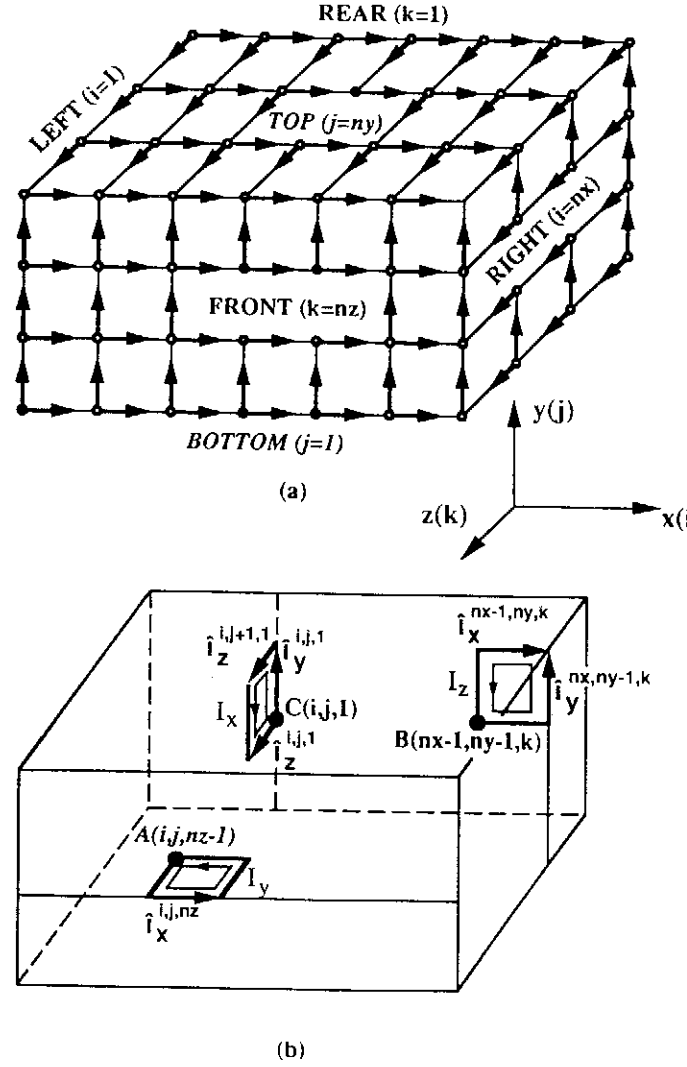

Figure 2 Model for the derivation of iterative loop current equations for the outer nodes of a parallelepiped sub-region.
(a) Line currents on the sub-region boundaries, i.e., left, right, bottom, top, rear and front surfaces;
(b) Three outer nodes: A(i,j,n_z-1), B(n_x-1,n_y-1,k) and C(i,j,1) and the boundary line currents involved in their loop current equations.

In Fig.2(b), the y-loop at A(i,j,nz-1), the z-loop at B(nx-1,ny-1,k) and the x-loop at C(i,j,1) are shown as representative of each category. The boundary line

currents involved around the loop are indicated by arrows; the unmarked line currents need to be decomposed into the loop currents. To illustrate the formulation of the method, the z-loop current equation at node B is derived in detail.

From Eq.(5), the z-loop equation at B(nx-1,ny-1,k) can be written as

$$R_x^{nx-1,ny-1,k}\hat{i}_x^{nx-1,ny-1,k}+R_y^{nx,ny-1,k}\hat{i}_y^{nx,ny-1,k}-R_x^{nx-1,ny,k}\hat{i}_x^{nx-1,ny,k}-R_y^{nx-1,ny-1,k}\hat{i}_y^{nx-1,ny-1,k}=emf_z^{nx-1,ny-1,k} \quad (8)$$

where line currents $\hat{i}_x^{nx-1,ny,k}$ and $\hat{i}_y^{nx,ny-1,k}$ have known values, and $\hat{i}_x^{nx-1,ny-1,k}$ and $\hat{i}_y^{nx-1,ny-1,k}$ are unknown. Using Eqs.(3) and (4), the unknown currents $\hat{i}_x^{nx-1,ny-1,k}$ and $\hat{i}_y^{nx-1,ny-1,k}$ can be expressed as

$$\hat{i}_x^{nx-1,ny-1,k}=-I_y^{nx-1,ny-1,k}+I_y^{nx-1,ny-1,k-1}+I_z^{nx-1,ny-1,k}-I_z^{nx-1,ny-2,k} \quad (9)$$

and

$$\hat{i}_y^{nx-1,ny-1,k}=-I_z^{nx-1,ny-1,k}+I_z^{nx-2,ny-1,k}+I_x^{nx-1,ny-1,k}-I_x^{nx-1,ny-1,k-1} \quad (10)$$

respectively. After substituting Eqs.(9) and (10) into Eq.(8) and rearranging it, $I_z^{nx-1,ny-1,k}$ can be readily found as

$$I_z^{nx-1,ny-1,k}=[emf_z^{nx-1,ny-1,k}+R_x^{nx-1,ny,k}\hat{i}_x^{nx-1,ny,k}-R_y^{nx,ny-1,k}\hat{i}_y^{nx,ny-1,k}+R_x^{nx-1,ny-1,k}(I_z^{nx-1,ny-2,k}+I_y^{nx-1,ny-1,k}-I_y^{nx-1,ny-1,k-1})+R_y^{nx-1,ny-1,k}(I_z^{nx-2,ny-1,k}+I_x^{nx-1,ny-1,k}-I_x^{nx-1,ny-1,k-1})]/(R_x^{nx-1,ny-1,k}+R_y^{nx-1,ny-1,k}) \quad (11)$$

Using a similar procedure, other loop current equations at the outer nodes listed in Table 1 can be derived.

What complicates the loop current derivation at the outer nodes is the fact that loop currents are the iterative variables in the impedance network method whereas line currents are used as the boundary values. The reason for this is that a loop current is not a physical but an imaginary parameter which only facilitates the iterative calculation. Consequently, the loop currents obtained from the whole region analysis are not directly usable for the boundary formulation of the sub-region analysis.

Outer Node Location	Loop Current	Index Range	Boundary Line Currents Used
Right Surface (i=nx-1)	I_y	$2\le j\le ny-1,\ 2\le k\le nz-2$	$\hat{i}_z^{nx,j,k}$
	I_z	$2\le j\le ny-2,\ 2\le k\le nz-1$	$\hat{i}_y^{nx,j,k}$
Top Surface (j=ny-1)	I_x	$2\le i\le nx-1,\ 2\le k\le nz-2$	$\hat{i}_z^{i,ny,k}$
	I_z	$2\le i\le nx-2,\ 2\le k\le nz-1$	$\hat{i}_x^{i,ny,k}$
Front Surface (k=nz-1)	I_x	$2\le i\le nx-1,\ 2\le j\le ny-2$	$\hat{i}_y^{i,j,nz}$
	I_y	$2\le i\le nx-2,\ 2\le j\le ny-1$	$\hat{i}_x^{i,j,nz}$
Left Surface (i=1)	I_y	$2\le j\le ny-1,\ 2\le k\le nz-1$	$\hat{i}_x^{1,j,k}, \hat{i}_x^{1,j,k+1}, \hat{i}_z^{1,j,k}$
	I_z	$2\le j\le ny-1,\ 2\le k\le nz-1$	$\hat{i}_x^{1,j,k}, \hat{i}_x^{1,j,k+1}, \hat{i}_y^{1,j,k}$
Bottom Surface (j=1)	I_x	$2\le i\le nx-1,\ 2\le k\le nz-1$	$\hat{i}_y^{i,1,k}, \hat{i}_y^{i,1,k+1}, \hat{i}_z^{i,1,k}$
	I_z	$2\le i\le nx-1,\ 2\le k\le nz-1$	$\hat{i}_x^{1,1,k}, \hat{i}_y^{i,1,k}, \hat{i}_y^{i+1,1,k}$
Rear Surface (k=1)	I_x	$2\le i\le nx-1,\ 2\le j\le ny-1$	$\hat{i}_y^{i,j,1}, \hat{i}_z^{i,j,1}, \hat{i}_z^{1,j+1,1}$
	I_y	$2\le i\le nx-1,\ 2\le j\le ny-1$	$\hat{i}_x^{i,j,1}, \hat{i}_z^{i,j,1}, \hat{i}_z^{i+1,j,1}$
X-Edge (j=ny-1,k=nz-1)	I_x	$2\le i\le nx-1$	$\hat{i}_y^{i,ny-1,nz}, \hat{i}_z^{i,ny,nz-1}$
Y-Edge (i=nx-1,k=nz-1)	I_y	$2\le j\le ny-1$	$\hat{i}_x^{nx-1,j,nz}, \hat{i}_z^{nx,j,nz-1}$
Z-Edge (i=nx-1,j=ny-1)	I_z	$2\le k\le nz-1$	$\hat{i}_x^{nx-1,ny,k}, \hat{i}_y^{nx,ny-1,k}$

Table 1 Summary of outer nodes and the boundary line currents involved in the loop current equations.

Verification

A solution for a double-layered sphere is used to verify the formulation and accuracy of the sub-region analysis. The sphere has radii of 0.15 m and 0.25 m, and electric conductivities of 1 S/m and 0.5 S/m for its inner and outer layers, respectively, and is placed in a uniform 60 Hz magnetic field in free space. An analytical solution is elementary for this problem and hence can be used to check the numerical results. The computation accuracy is evaluated by an average relative error defined as [8]:

$$\delta=\frac{\overline{\Delta J_\phi}^*}{\bar{J}_\phi}=\frac{\sum_{i,j,k}\left|J_\phi^*(i,j,k)-J_\phi(i,j,k)\right|}{N\bar{J}_\phi} \quad (12)$$

in which the summation is performed over all the non-air cells and N is the number of cells. J_ϕ^* and J_ϕ are the numerical and analytical magnitudes of the current density (the only component is in the ϕ direction), and a bar denotes the average value.

The verification is conducted in three steps. In the first step, computations are performed for the whole sphere. In the second step, one eighth of the sphere is considered for a sub-region analysis where the boundary values in the planes of x=0, y=0 and z=0 as shown in Fig.3 need to be assigned. The computational cell size is halved in each dimension, resulting in roughly the same number of cells as for the whole sphere. To examine the effect due to the error in boundary values, the computation of this eighth sphere is performed for two cases. For the first case, the numerical results from the whole sphere, and for the

second case the analytical results, are used as the boundary values. In the final step, a cubical region partially embeded in one eighth of the sphere (see Fig.4) is chosen for another stage of sub-region analysis and the cell size is again halved. The boundary values on the six surfaces of this cube are taken from the numerical results from case one and two, and from the analytical solution.

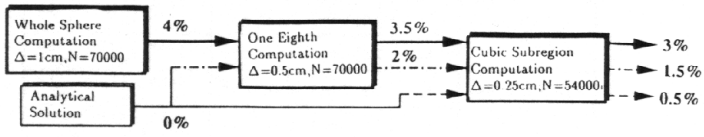

Figure 3 Eighth of a double-layered sphere with a partially embeded cubical sub-region (the mid-horizontal cross-section of the cube shaded.

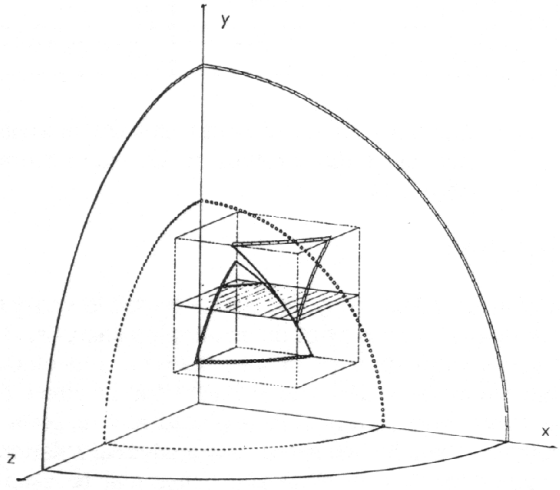

Figure 4 The relative errors in the computations of a double-layered sphere.

The error for each case is illustrated in Fig.4. The average error in the numerical results after each stage of sub-region cell size halving is reduced to at least half of the larger cell value, provided the boundary values used are accurate. This is, understandably, due to the use of finer meshes which model the interface better. The distributions of the induced current densities computed with cells of 1 cm, 0.5 cm and 0.25 cm on the mid-cross section of the cubical sub-region are shown in Fig.5, illustrating a higher spatial resolution with a finer cell modeling. On the other hand, the computational error is much larger when the numerical results are used as the boundary than when the analytical values are used. For instance, the error in the computation for one eighth of the sphere is 3.5% in the case of using the numerical boundary values as compared to 2% when using analytical boundary values. This indicates that the improvement in computation accuracy obtained from one or multi-stage sub-region analysis will be limited unless the whole region analysis is reasonably accurate.

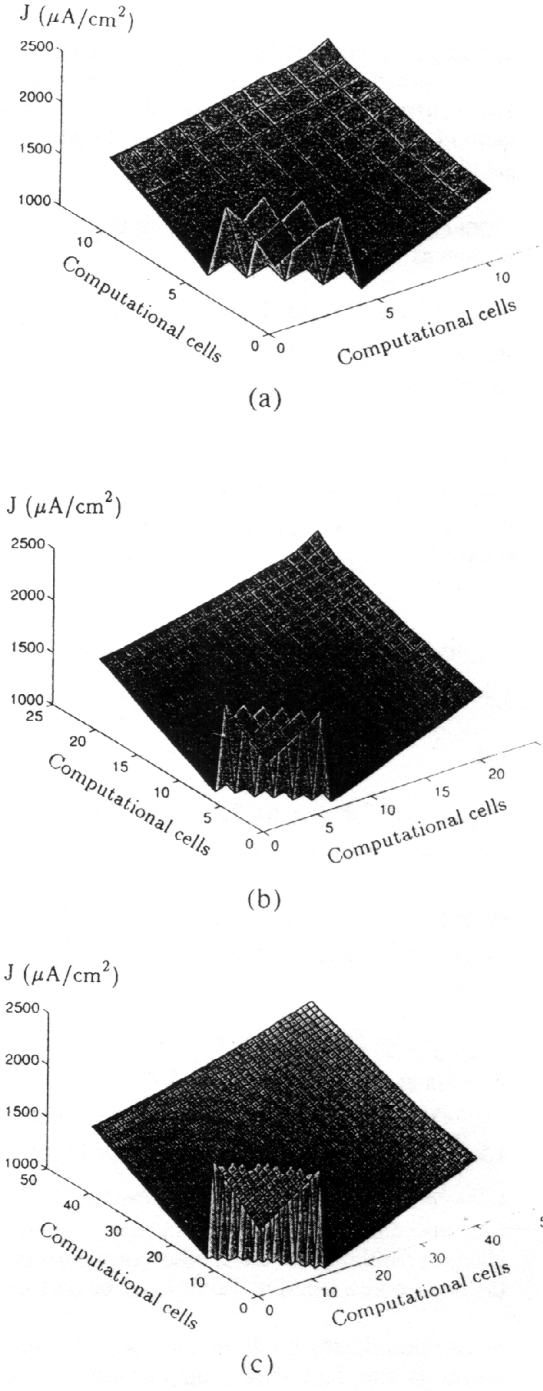

Figure 5 Distribution of the induced electric current density on the surface corresponding to the shaded cross-section in Fig.4, from the computations of
(a) whole sphere using 1 cm cell size;
(b) one eighth of the sphere using 0.5 cm cell size;
(c) cubical sub-region one eighth of the sphere using 0.25 cm cell size.

Sub-Region Analysis of Human Head

To illustrate the application of the above-described approach to sub-region analysis, electric currents and fields induced in the human head by a uniform 60 Hz magnetic field of 1 T directed from the back to the front are computed. The anatomically based man models developed at the University of Utah [4] are used in this computation. The data base of the man models was constructed from a cross-section anatomy book [9]. In creating this data base, a roughly quarter-inch grid (0.665cm) was first divided on each of the transverse body cross-sections which are equally spaced by the grid size. An electric conductivity was assigned to each of such cubical cells, according to the tissue type. Isotropic properties of muscle were used. The conductivity matrix for the body volume and its surrounding space has 90X48X268, i.e., about 1.16 million elements. Since this requires a memory too large for most readily accessible computers, the data for 2X2X2 = 8 cells are combined to form a smaller matrix of 45X24X134 with 144 720 elements. This half-inch model is used in the whole body computation, while the quarter-inch model is used in the computation of the head-region starting from the neck. The boundary values on the neck cross-section are obtained by interpolating (proportionally to the grid surface) the line current densities from the whole body computation.

The average and maximum values of the calculated electric currents and fields induced in the head are listed in Table 2 for three computation cases. The electric field strength is calculated by multiplying the current density by the corresponding conductivity for each cell. First, as case 1 the whole body response of the man model is used with the coarse grid (1/2-inch cell size). A head region is then separated from the neck up and calculations using the finer model (1/4-inch cell size) are performed for two cases which differ by the boundary values assumed on the neck cross-section, The results obtained from case 1 are used in case 2 and null values are used in case 3. Therefore, case 2 takes into account the effects of the whole body, whereas case 3 neglects current flowing between the head and the rest and thus only models an isolated detached head.

From Table 2, it can be seen that the maximum current density and field intensity for smaller computational cells are 2-3 times higher than those of case 1, though the average values are very close to those obtained with the coarser grid. It is expected that the ratio of the maximum to the average for both the current and field in the head would be even larger if the head were modeled with finer computational cells. Secondly, the differences in the average and the maximum values between case 2 and 3 are significant, indicating that the current flow between the head and the rest of the body should not be neglected. It is found that the densities of the current flow through the neck are of the order of 1,000 $\mu A/cm^2$, that is, about half of the maximum or 5 times the average value in the head region. Understandably, for an exposure to a field directed from the back to the front, much smaller electric currents and fields are induced in a detached head than in the head attached to the body because of the smaller coronal cross-sections. If the magnetic field is applied along the body vertical axis (head to toe), the difference between these two cases would be smaller.

The spatial distribution of induced current density on two cross-sections are presented in Fig.6 and Fig.7 for case 2 and 1, respectively. The cross-sections chosen are the frontal passing through the ears and the transverse through the nose. The distribution obtained with the smaller computational cells reflects more anatomical details than with the coarse grid. For instance, a realistic shape of the nose and a distinctive air cavity of the pharynx can be seen in Fig.6a. The difference between the current density in the facial bones (low conductivity) and the facial muscles (high conductivity) is also exhibited in Fig.6. Within the cranial cavity (brain), a relatively uniform current density is shown in both Fig.6 and Fig.7.

Computations Cases	Current Density ($\mu A/cm^2$)		E-Field (V/M)	
	Aver-age	Maxi-mum	Aver-age	Maxi-mum
Case 1: Whole Body Analysis (Δ = 1/2-inch, N = 144,700)	191	1440	14.0	105
Case 2: Head Sub-Region Analysis (Δ = 1/4-inch, N = 35,900)	206	2000	13.7	296
Case 3: Detached Head Analysis (Δ = 1/4-inch, N = 35,900)	161	1050	11.3	65.2

Table 2 Comparison of various computation cases of modeling the electric current and field induced in the human head by a 60 Hz uniform magnetic field of 1 T directed from the back to the front.

Conclusions

It is demonstrated that in calculations of the induced electric current distribution in a 3D - model of the heterogeneous human body, the impedance network method coupled with the sub-region analysis approach is a practicle way of dealing with theconflicting requirements of modeling resolution and computation manageability. Using one or multiple stages of sub-region analysis, a body region of interest can be dealt with in a "zoom" manner without resulting in an excessively large number of computation cells. Of course, a correspondingly fine model of man is required for this purpose. Our example

of the head analysis shows that the 1/4-inch man model results in spatial current distribution with a much higher resolution than those with the 1/2-inch model. However, to properly model some organs, such as eyes, an even finer anatomical model is needed. Computational accuracy can be significantly improved if accurate values of curents at boundaries of the sub-region are known and used in the analysis.

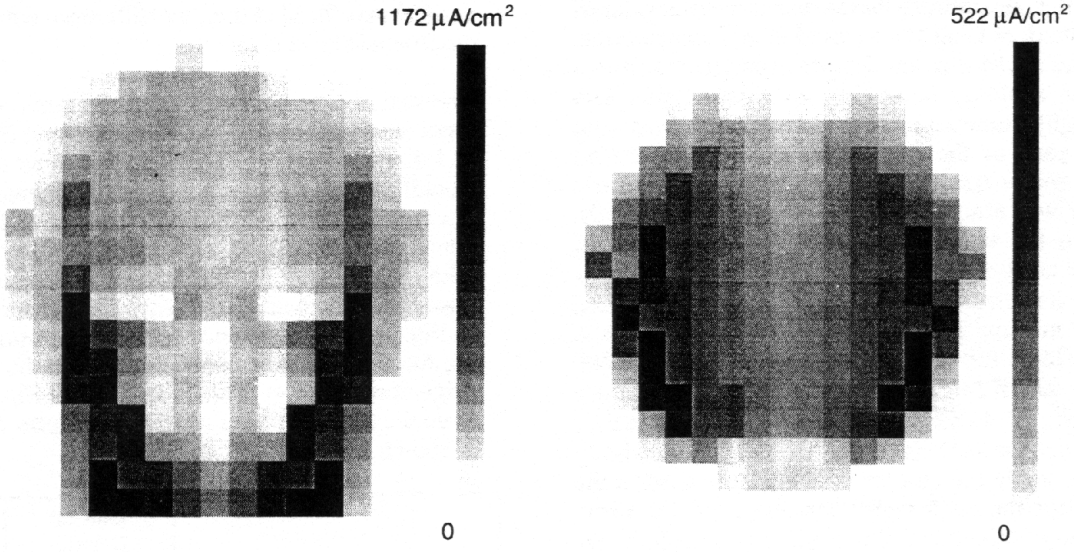

Figure 6 Spatial distribution of the current density induced in the human head on
(a) the frontal cross-section passing the ears and
(b) the transverse cross-section passing through the nose, obtained from the whole body analysis using 1/2-inch man model.

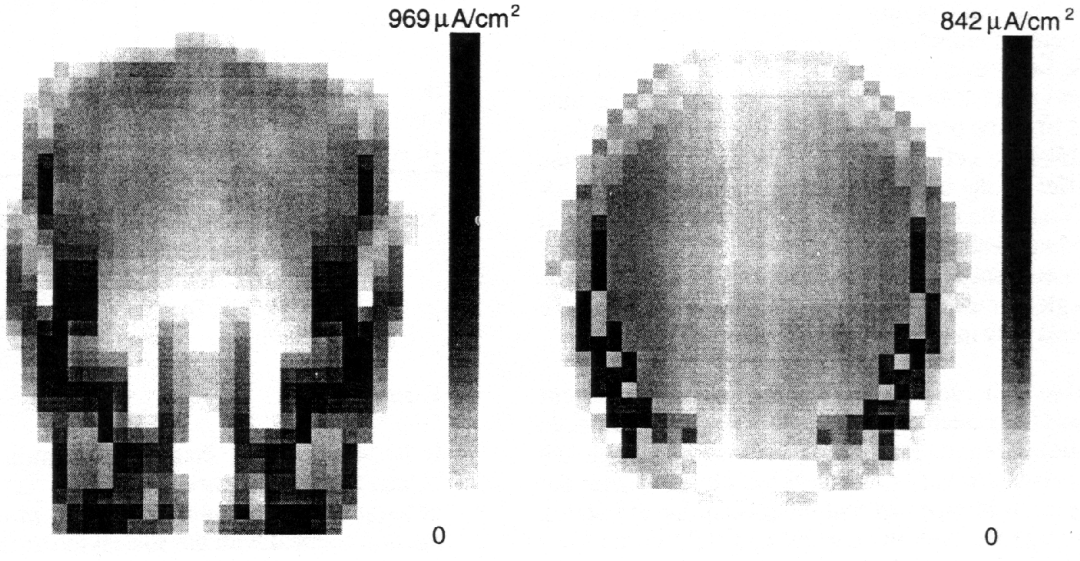

Figure 7 Spatial distribution of the current density induced in the human head on
(a) the frontal and
(b) the transverse cross-sectionpassing through the nose, obtained from the head subregion analysis using 1/4-inch man model.

Acknowledgement

This work is supported by a strategic grant from the Natural Sciences and Engineering Research Council of Canada and a grant from the U.S. National Institutes of Health through a contractual agreement with the University of California, Riverside. The authors also wish to thank Dr. O.P. Gandhi and Ms. C. Furse of the University of Utah for their generous assistance.

References

[1] G. Theriault, "Cancer risks due to exposure to electromagnetic fields", *Recent Results in Cancer Res.*, Vol.120, pp.166-180, 1990.

[2] S.F. Cleary, "In vitro studies: low frequency electromagnetic fields", *Proc. Sci. Workshop on the Health Effects of Electromagnetic Radiation on Workers*, U.S.Dept. of Health and Human Services, Cincinnati, OH, Publ. No.91-111, pp.47-89, 1991.

[3] M.A. Stuchly, "Applications of time-varying magnetic fields in medicine", *CRC Crit. Rev. Biomed. Eng.*, vol.18, pp.89-124, 1990.

[4] O.P. Gandhi and J.Y. Chen, "Numerical dosimetry at power-line frequencies using anatomically based models", *Bioelectromagn.*, Supplement No.1, pp.43-60, 1992.

[5] P.J. Dimbylow, "The calculation of induced currents and absorbed power in a realistic, heterogeneous model of the lower leg for applied electric fields from 60 Hz to 30 MHz", *Phys. Med. Biol.*, Vol.33, No.12, pp.1453-1468, 1988.

[6] P.J. Dimbylow, "Finite-difference time-domain calculations of SAR in a realistic heterogeneous model of the head for plane-wave exposure from 600 MHz to 3 GHz", *Phys. Med. Biol.*, Vol.36, No.8, pp.1075-1089, 1991.

[7] N.Orcutt and O.P. Gandhi, "A 3-D impedance method to calculate power deposition in biological bodies subjected to time varying magnetic fields, *IEEE Trans.Biomed. Eng.*, vol.BME-35, pp.577-587, 1988.

[8] W. Xi, M.A. Stuchly and O.P. Gandhi, "Induced electric currents in models of man and rodents from 60 Hz Magnetic fields", Accepted to *IEEE Trans. Biomed. Eng.*, 1994.

[9] A.C. Eycleshymer and D.M. Schoemaker, *A Cross-Section Anatomy*, New York: Appleton, 1911.